Dynamics of Atmospheres and Oceans 75 (2016) 78–90

Contents lists available at ScienceDirect

Dynamics of Atmospheres and Oceans

journal homepage: www.elsevier.com/locate/dynatmoce

# MJO prediction skill, predictability, and teleconnection impacts in the Beijing Climate Center Atmospheric General Circulation Model

Jie Wu [a,b], Hong-Li Ren [b,*], Jinqing Zuo [b], Chongbo Zhao [b], Lijuan Chen [b], Qiaoping Li [b]

[a] College of Atmospheric Sciences, Nanjing University of Information Science and Technology, Nanjing 210044, China
[b] Laboratory for Climate Studies, National Climate Center, China Meteorological Administration, Beijing 100081, China

ARTICLE INFO

*Article history:*
Received 8 March 2016
Received in revised form 2 June 2016
Accepted 11 June 2016
Available online 14 June 2016

*Keywords:*
MJO
BCC_AGCM
Prediction
Teleconnections

ABSTRACT

This study evaluates performance of Madden–Julian oscillation (MJO) prediction in the Beijing Climate Center Atmospheric General Circulation Model (BCC_AGCM2.2). By using the real-time multivariate MJO (RMM) indices, it is shown that the MJO prediction skill of BCC_AGCM2.2 extends to about 16–17 days before the bivariate anomaly correlation coefficient drops to 0.5 and the root-mean-square error increases to the level of the climatological prediction. The prediction skill showed a seasonal dependence, with the highest skill occurring in boreal autumn, and a phase dependence with higher skill for predictions initiated from phases 2–4. The results of the MJO predictability analysis showed that the upper bounds of the prediction skill can be extended to 26 days by using a single-member estimate, and to 42 days by using the ensemble-mean estimate, which also exhibited an initial amplitude and phase dependence. The observed relationship between the MJO and the North Atlantic Oscillation was accurately reproduced by BCC_AGCM2.2 for most initial phases of the MJO, accompanied with the Rossby wave trains in the Northern Hemisphere extratropics driven by MJO convection forcing. Overall, BCC_AGCM2.2 displayed a significant ability to predict the MJO and its teleconnections without interacting with the ocean, which provided a useful tool for fully extracting the predictability source of subseasonal prediction.



## 1. Introduction

It is well known that the predictability limit of weather forecasts is between two and three weeks. Beyond that, the initial errors grow quickly and become so large that overwhelm the useful signals in the forecast. In contrast, for seasonal predictions, the predictability mostly comes from the lower boundary and some influences external to the atmosphere (Shukla et al., 2000), such as oceans, soil moisture, land use, and sea ice. Nowadays, the extended-range forecast, as the gap between the weather forecasts and seasonal predictions, has received increasing attention because of large needs of society (Waliser et al., 2006).

* Corresponding author at: National Climate Center, China Meteorological Administration, 46 Zhongguancun, Haidian District, Beijing 100081, China.
*E-mail address:* renhl@cma.gov.cn (H.-L. Ren).

http://dx.doi.org/10.1016/j.dynatmoce.2016.06.001

The Madden–Julian oscillation (MJO) is the most prominent mode of intraseasonal variability in the tropics (Madden and Julian, 1971, 1972) and plays a critical role in bridging weather and climate (Zhang, 2013). The MJO is typically characterized by a spatial structure of zonal wavenumber one with large-scale signals in the atmospheric circulation, deep convection, and other variables propagating slowly eastwards (at approximately 5 m/s) from Indian to Pacific oceans (Zhang, 2005). The MJO modulates tropical cyclone (TC) genesis and activity (Vitart et al., 2010; Fu and Hsu, 2011), influences global weather and climate variability (Donald et al., 2006), impacts on extratropical teleconnections such as the Arctic Oscillation (AO) and North Atlantic Oscillation (NAO; Cassou, 2008), and also affects climate variability over longer timescales, such as the El Niño-Southern Oscillation (ENSO; Kessler and Kleeman, 2000; Wang et al., 2011). In addition, the MJO has an important impact on the onset and break of the summer monsoon and precipitation over East Asia via stimulating of anomalous meridional teleconnection between the tropics and middle latitudes, and changing the northward transportation of low-level moisture (Jeong et al., 2008; Jia et al., 2011; Jia and Liang, 2013; Qi and Zhang, 2015). Recently, lots of theoretical researches have advanced the fundamental dynamics of MJO (Li, 2014), such as its scale selection (Li and Zhou, 2009), initialization (Zhao et al., 2013; Li et al., 2015), and moisture asymmetry construction (Hsu and Li, 2012, 2014), increasing our knowledge and references in understanding the predictability of the MJO and intraseasonal variability.

Therefore, as the MJO has a significant influence on the climate and weather events, the effective prediction of the MJO could fill in the predictability gap between weather forecasts and seasonal predictions. Over the last decade, there has been a significant improvement in MJO prediction skill and the potential predictability of dynamical models (Ren et al., 2015). Seo et al. (2009) evaluated the MJO forecasts from the National Centers for Environmental Prediction (NCEP) Climate Forecast System (CFS) and showed that this system has useful MJO prediction skill out to 10–15 days. Wang et al. (2014) further found that such a useful MJO prediction skill could be extended to 20 days by using CFS version 2. Rashid et al. (2011) examined the performance of the Predictive Ocean–Atmosphere Model for Australia (POAMA) and showed that the useful MJO forecast can extend to 21 days. More recently, Hudson et al. (2013) found that the POAMA-2 multi-week forecast system had further improved MJO prediction skill (out to 23 days) by applying a coupled-breeding initialization approach. Meanwhile, Kang and Kim (2009) and Kang et al. (2014) showed that by using an empirical singular vector (ESV) perturbation method, the MJO prediction limit of the Seoul National University coupled general circulation model (SNU CGCM) could be increased from 20 to 22 days. Fu et al. (2013) showed that the forecasting skills of MJO major modes can reach 13, 25, and 28 days in the GFS (Global Forecast System) atmosphere-only model, the CFSv2, and UH (University of Hawaii) coupled models, respectively, during the DYNAMO (Dynamics of the MJO) period. Also, major progress had been made by the European Center for Medium-Range Weather Forecasts (ECMWF) since 2002, with an evident increase in prediction skill (of about 1 day per year) to 30 days by 2012 (Vitart et al., 2007; Vitart and Molteni 2010; Vitart, 2014).

Recently, several studies have focused on characterizing the predictability of the MJO using contemporary general circulation models. Pegion and Kirtman (2008) showed that the predictability of the MJO could be extended beyond 45 days by estimating the predictability of the NCEP CFS hindcast data. Furthermore, Neena et al. (2014) made two estimates of MJO predictability based on the single-member and ensemble-mean methods, which showed the predictability limit of MJO to be around 20–30 days and 35–45 days, respectively. This study indicated that more skillful MJO forecasts could be generated from improvements in the dynamical models and ensemble prediction systems. These studies were almost all based on CGCMs that included air–sea coupling processes which may positively contribute to better simulations of both the MJO dynamics and propagation (Fu et al., 2013). However, whether the introduction of air–sea coupling can significantly improve MJO prediction skill remains controversial (Hendon 2000; Chou and Hsueh 2010), despite it being much more expensive to run a full CGCM than its atmospheric component in an operational system.

In this study, we focus on an atmospheric GCM rather than the CGCM to examine its performance in predicting the MJO. We also evaluate the predictability of the MJO using a unique daily-initialized hindcasts dataset generated by the Beijing Climate Center Atmospheric General Circulation Model version 2.2 (BCC_AGCM2.2), which has been applied to the Dynamical Extended-Range Forecasting (DERF) in the BCC operational prediction system. This AGCM has shown a much-improved performance in monthly predictions of the surface air temperature and precipitation over China, and also in the simulations of the MJO and AO, when compared with the earlier version of the model (Wu et al., 2010; He et al., 2014; Zhao et al., 2014, 2015; Zuo et al., 2016). This study also aims to increase our understanding of the MJO impacts through extratropical teleconnections, which provide an important reference when making predictions over subseasonal timescales. The remainder of the paper is organized as follows. Section 2 describes the datasets and methodology used. The overall prediction skill of the MJO is evaluated in Section 3, and the detailed analysis of the amplitude and propagation characteristics of the MJO is given in Section 4. Then, evaluations of the predictability in the model are presented in Section 5, and Section 6 analyzes the lagged relationship between the MJO and Northern Hemisphere teleconnection. Finally, conclusions and discussions are presented in Section 7.

## 2. Data and methodology

### 2.1. The hindcast data

Our analysis is based on the hindcasts from the BCC_AGCM2.2 model with triangular 106 (T106) horizontal resolution and 26 vertical levels (T106L26). The initialization scheme of hindcasts is nudging the atmosphere condition towards the National Centers for Environmental Prediction/National Center for Atmospheric Research (NCEP/NCAR) Reanalysis-1 data

(Kalnay et al., 1996) at an interval of six hours. The model was driven by the NOAA (National Oceanic and Atmospheric Administration) OISST (Optimum Interpolation Sea Surface Temperature) of the most recent week, which will remain constant through the forecast period. We analyze 50-day hindcasts that were initialized daily from 1 January 1991 to 31 December 2010. For each initial date, one forecast is made every six hours from 00Z, 06Z, 12Z, and 18Z, forming a daily ensemble with four initial-value members. The 200-hPa zonal wind (U200), 850-hPa zonal wind (U850), 500-hPa geopotential height (Z500), and outgoing longwave radiation (OLR) are used in the analysis. All data are interpolated onto a grid with a horizontal resolution of $2.5^\circ \times 2.5^\circ$. This model is already being used for operational climate prediction in BCC and its real-time MJO operational prediction products aredaily updated on the website (http://cmdp.ncc-cma.net/Monitoring/moni_mjo.php). Therefore, this dataset allows a comprehensive and reliable evaluation of the MJO prediction performance with continuous model climatology.

### 2.2. Calculation of the RMM indices

Although there are many definitions of the MJO, we identify the MJO based on a real-time multivariate MJO (RMM) indices described by Wheeler and Hendon (2004), (hereafter WH04). First of all, we calculate the intraseasonal anomalies of the observed and predicted data following Lin et al. (2008) and Wang et al. (2014). The OLR data from the NOAA (Liebmann and Smith 1996), the U850 and U200 values from the NCEP/NCAR-1 reanalysis dataset are used as the observations. For the predicted data, the anomalies are calculated relative to the model climatology for 1991–2010 using hindcast data, which is a function of both initial calendar date and lead time. Then, the interannual component is removed by subtracting the previous 120-day mean, which combines the observations and the forecast before the target date. But for the observed data, the intraseasonal anomalies are calculated by removing the observed climatology, which is only a function of the calendar date. Thereafter, the three intraseasonal anomaly fields are averaged between 15°S and 15°N, and normalized using the observed standard deviation of each field.

In this study, we use the same MJO-related spatial structures (eigenvectors) and variances (eigenvalues) as WH04, available from http://cawcr.gov.au/staff/mwheeler/maproom/RMM/eofcode.htm. We project the daily observational data and model hindcasst data onto these observation-derived spatial structures to get both verification and model hindcast RMM values. It should be noted that because of differences in climatology definition and the way that the interannual variability is removed, these verification RMM values are not the exactly same as those of WH04, but their differences are very small.

### 2.3. Measures of the prediction skill

The MJO prediction skill is measured using the bivariate anomaly correlation coefficient (COR), bivariate anomaly root mean square error (RMSE), and mean square skill score (MSSS), which are defined as

$$\mathrm{COR}(\tau) = \frac{\sum_{i=1}^{N}[a_{1i}(t)b_{1i}(t) + a_{2i}(t)b_{2i}(t)]}{\sqrt{\sum_{i=1}^{N}[a_{1i}^2(t) + a_{2i}^2(t)]}\sqrt{\sum_{i=1}^{N}[b_{1i}^2(t) + b_{2i}^2(t)]}} \tag{1}$$

$$\mathrm{RMSE}(\tau) = \sqrt{\frac{1}{N}\sum_{i=1}^{N}\{[a_{1i}(t) - b_{1i}(t)]^2 + [a_{2i}(t) - b_{2i}(t)]^2\}} \tag{2}$$

$$\mathrm{MSSS}(\tau) = [1 - \frac{\mathrm{MSE_f}(\tau)}{\mathrm{MSE_c}}] = [1 - \frac{\frac{1}{N}\sum_{i=1}^{N}\{[a_{1i}(t) - b_{1i}(t)]^2 + [a_{2i}(t) - b_{2i}(t)]^2\}}{\frac{1}{N}\sum_{i=1}^{N}[a_{1i}^2(t) + a_{2i}^2(t)]}] \tag{3}$$

where $a_{1i}(t)$ and $a_{2i}(t)$ are the observed RMM1 and RMM2 at day $t$, and $b_{1i}(t)$ and $b_{2i}(t)$ are their corresponding forecasts, for the $i$th forecast with a $\tau$-day lead. Here, N is the number of forecasts (Lin et al., 2008). The COR, RMSE, and MSSS are calculated using the intraseasonal prediction anomalies of the four-member ensemble mean on each initial day.

### 2.4. MJO predictability estimation method

The predictability of the MJO in the hindcast is measured using two approaches (see Neena et al., 2014): the single-member predictability estimate and the ensemble-mean predictability estimate. For the former one, a single member of the

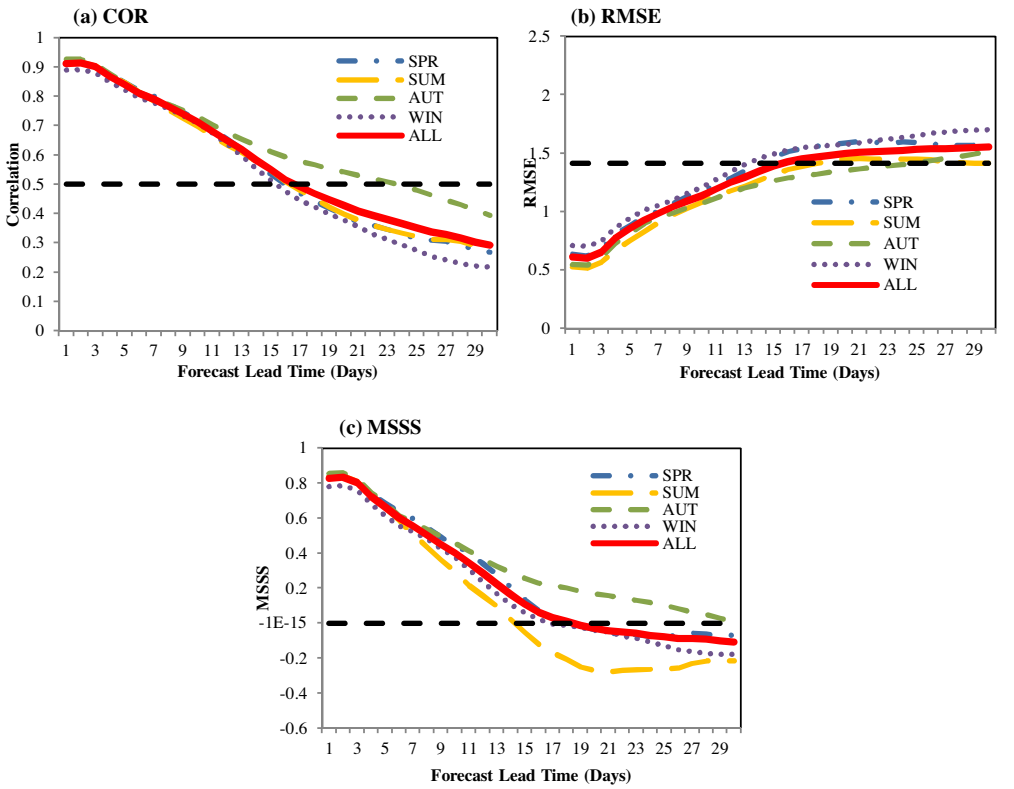


**Fig. 1.** (a) Correlation coefficient (COR), (b) root-mean-square error (RMSE), and (c) mean square skill score (MSSS) for bivariate RMM indices in each season. The horizontal dashed lines are 0.5 in (a), $\sqrt{2}$ in (b), and 0 in (c). The blue line, yellow line, green line, purple line, and red line represent the skills in spring, summer, autumn, winter, and all of the years, respectively (for interpretation of the references to color in this figure legend, the reader is referred to the web version of this article.)

ensemble is considered as the control hindcast, and every other ensemble member is regarded as a perturbed hindcast. The mean-square error for each lead day $j$ is derived from Eq. (4)

$$\langle E_j^2 \rangle = \frac{1}{N \times m_1} \sum_{i=1}^{N} \sum_{pairs} [(\mathrm{RMM1}_{ij}^{control} - \mathrm{RMM1}_{ij}^{perturb})^2 + (\mathrm{RMM2}_{ij}^{control} - \mathrm{RMM2}_{ij}^{perturb})^2] \quad (4)$$

Here, $m_1$ is the number of possible control–perturbed pairs for a given initial value and $N$ gives the total number of initial values. The mean signal for each lead day $j$ [Eq. (5)] is computed over a total $N \times nk$ control cases, where $nk$ indicates the ensemble size.

$$\langle S_j^2 \rangle = \frac{1}{N \times nk} \sum_{i=1}^{N} \sum_{nk} [(\mathrm{RMM1}_{ij}^{control})^2 + (\mathrm{RMM2}_{ij}^{control})^2] \quad (5)$$

For the ensemble-mean predictability estimate, the error growth is estimated for a single member (control) and the ensemble mean over all of the other ensemble members (perturbed). Therefore, in calculating the mean-square error [Eq. (4)], $m_1$ takes the value of the ensemble size $nk$. The signal estimation is the same as that for the single-member predictability estimate. The estimate of MJO predictability is obtained from the lead time at which the error curve becomes as large as the signal one.

## 3. MJO prediction skills

In this section, we analyze the performance of the BCC_AGCM2.2 in predicting the MJO. Fig. 1 shows the bivariate COR, RMSE, and MSSS of the RMM indices for each season over the period 1991–2010. Overall, if 0.5 is taken as the baseline for useful COR skill, the MJO can be predicted out to a lead time of 16–17 days. In addition, there is a significant seasonal variation in prediction skill. The highest COR prediction skill occurred in autumn (September, October, and November: SON), when the number of days with useful COR skill reached 23, but only 15 days in spring (March, April, and May: MAM) and winter (December, January, and February: DJF). In summer (June. July, and August: JJA), the COR skill extended to about 16 days.

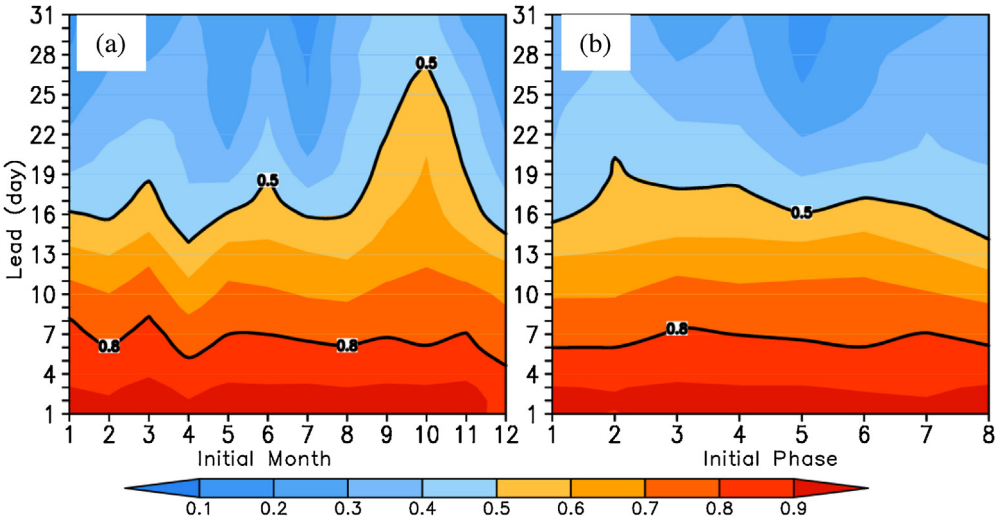


**Fig. 2.** MJO prediction skill of COR as a function of (a) initial calendar month and (b) MJO initial phase.

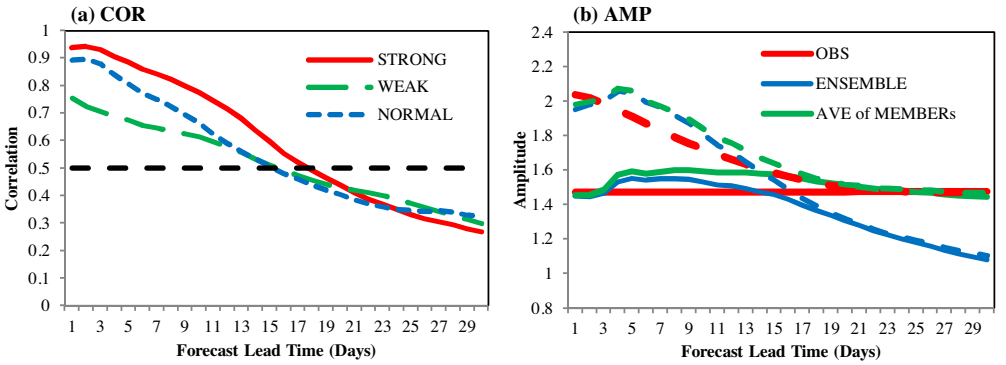


**Fig. 3.** (a) Bivariate RMM indices COR for initial strong, normal, and weak MJO cases (see text for definition of each case). (b) The evolution of MJO amplitude with lead time for initially strong MJO cases (dashed lines) and for all MJO cases (solid lines). Red curves are observations, blue curves are forecast ensemble means, and green curves are average amplitude of the four forecast members (for interpretation of the references to color in this figure legend, the reader is referred to the web version of this article.)

When we consider the RMSE and MSSS, the prediction skill of the RMM indices is also about, or more than, 16 days if we take $\sqrt{2}$ and 0 as the baselines of the RMSE and MSSS, respectively (Lin et al., 2008). These results indicate that, although the MJO prediction skill of the BCC_AGCM2.2 model may be less than that of some coupled models, such as ECMWF (Vitart, 2014) and CFSv2 (Wang et al., 2014), the skill of this model is actually comparable with, or even better than, other AGCMs, taking GFS's result for example (Fu et al., 2013).

The bivariate RMM COR skills are also calculated as a function of calendar month and initial phase. Fig. 2a shows that seasonal variations in the prediction skill are more than 13 days, with the highest COR skill in October (27 days) and the lowest in April (14 days). We note that the dependence of the prediction skill on the season is not consistent with other studies; for example, Rashid et al. (2011) found an improved RMM prediction skill in winter, but lower skill in summer. However, this result may be model dependent and requires further investigation. We also examined the dependence of prediction skill on the initial phase of the MJO, and found that it is generally higher in the predictions from phases 2–4, and lower from phases 1 and 8 (Fig. 2b). This result is consistent with other models such as GFDL (Geophysical Fluid Dynamics Laboratory) coupled model (Xiang et al., 2015), which clearly suggests that dynamical models are usually more skillful when MJO convection is located over the Indian Ocean at the initial time of forecasting.

## 4. The maintenance and propagation characteristics of the MJO

The dependence of the RMM COR skills on the initial amplitude of the MJO is further examined separately in Fig. 3a. A strong MJO case is defined as having an initial RMM amplitude ($\sqrt{RMM1^2 + RMM2^2}$) greater than $\sqrt{2}$, whereas a weak case is defined as having an initial amplitude of less than 1; otherwise the MJO is considered to be a normal case. The frequencies of the strong, normal, and weak MJO cases are about 40%, 25%, and 35%, respectively. Fig. 3a shows that the prediction skill

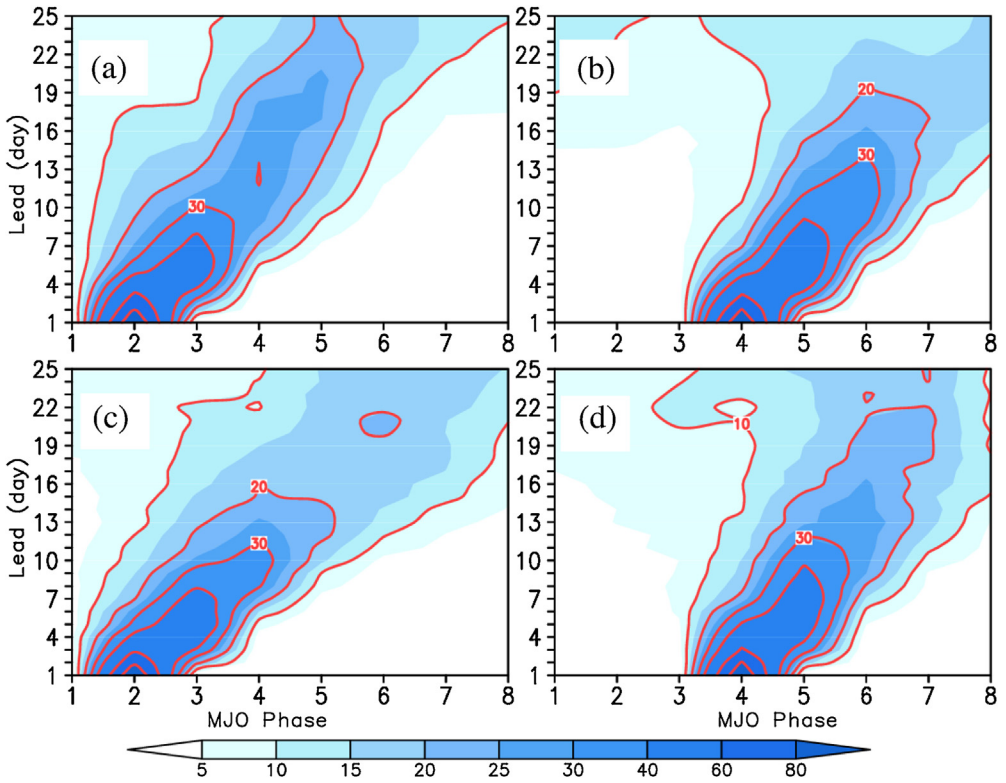


**Fig. 4.** Hovmoller diagram of the percentage of MJO events in a specific MJO phase as a function of lead time following an MJO initialized in phase 2 (a, c) and phase 4 (b, d). (a) and (b) show the eastward propagation in the observations, (c) and (d) show the eastward propagation of the MJO in the BCC_AGCM2.2 forecast. The red contours are the percentages of MJO events, same as the shaded and plotted at an interval of 10% (for interpretation of the references to color in this figure legend, the reader is referred to the web version of this article.)

is generally higher for the strong case, where the useful skill is extended by about 2 days compared with the weak case, and this is similar to previous studies in terms of both statistical and dynamical predictions (Lin et al., 2008; Rashid et al., 2011). For the weak case, the initial prediction skill is much lower, especially in the first three days, and the influence of the initial conditions can extend to more than 20 days.

The evolution of the amplitude of the RMM indices is compared in Fig. 3b for strong cases and all MJO cases. For the former one, the initial amplitude of the observed RMM indices decreases with time and approaches the value of the climatological amplitude ($\sqrt{2}$) after 20 days. The member-averaged amplitude of the forecasts is slightly smaller than the observations over the first 3 days, but shows a sudden rise at day 4 and remains a little larger than the observations throughout the 30-day forecast period, which indicates that the MJO amplitude in BCC_AGCM2.2 is comparable with the observations. For the four-member ensemble mean, the amplitude is progressively smaller than the individual members as the lead time increases, indicating the larger cancellation of uncorrelated errors among the forecast members. For the average of all MJO events, the observed amplitude holds the climatological value throughout the run, but for the forecast, the ensemble mean amplitude drops abruptly after 15 days. Therefore, it is reasonable to deduce that due to the cancellation of uncorrelated components of the MJO-related anomalies among forecast members, the ensemble mean is unable to maintain the initial MJO amplitude for a long period, especially after 15 days, which may restrict the prediction limit of the MJO. It is also worth noting that the prediction skill is much lower for the weak case, which may be related to deficiencies in the initialization scheme of the model.

To examine the MJO propagation features in the model hindcast, Fig. 4 shows the composites of the percentage of MJO events initialized in phase 2 (convection over the western Indian Ocean) and phase 4 (convection over the Maritime Continent), in which daily evolution has been calculated for the reanalysis and model hindcasts. In phase 2, the eastward propagation of the MJO in the model is similar to the observations over the first 15 days, but propagates faster than the reanalysis thereafter. For instance, the majority of MJO events in the reanalysis reach phase 5 on day 25, whereas the model reaches phase 7 or 8. In addition, there is less consistency in the eastward propagation of the MJO in the model when compared with the observations, especially after 20 days.

To further examine the evolution of the MJO-related physics, the time–longitude sections of the intraseasonal OLR (shaded) and U850 (contours) anomalies are shown in Fig. 5 for predictions initialized in phases 2 and 4. The zero lines of the U850 are highlighted by the red contours. It is clear that the speed of eastward propagation of the MJO convection and U850 anomalies is about 5 m/s in the observations, and the east wind extends much farther into the central Pacific and

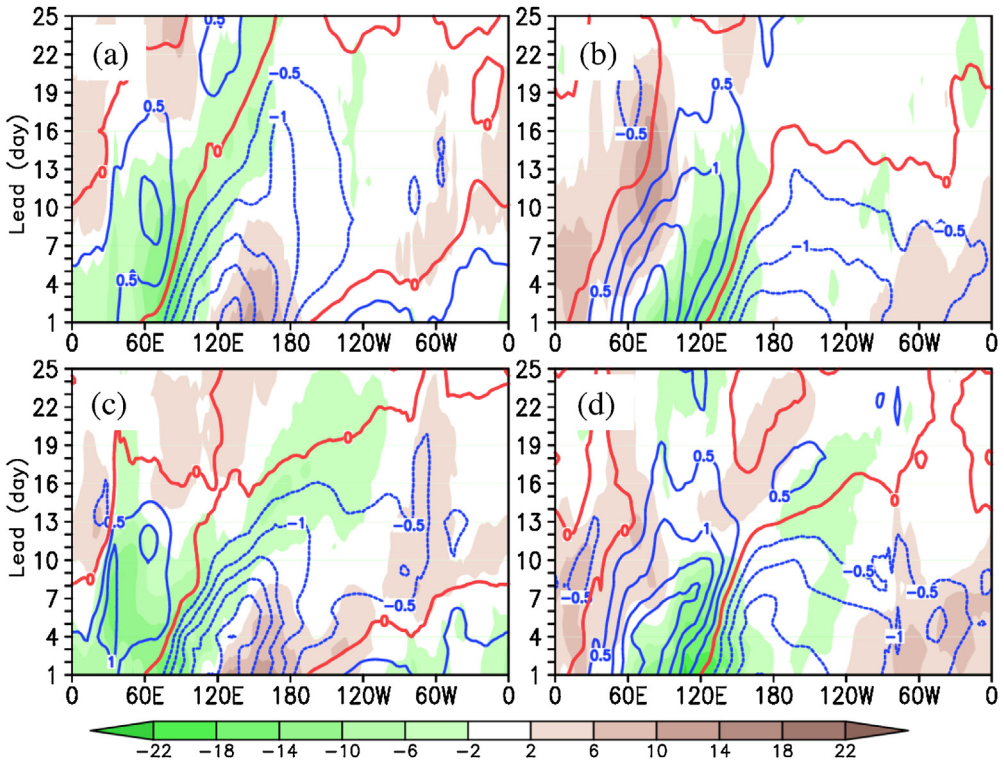


**Fig. 5.** Composite OLR (shading) and U850 (contours) anomaly for initial phase 2 (a, c) and phase 4 (b, d). (a) and (b) are observations whereas (c) and (d) are forecasts. The evolutions were started from observations at the initial time.

Western Hemisphere (Fig. 5a). The enhanced convection is located at the interface of the east and west wind of 850 hPa over the Indian Ocean, and in the west wind over the western Pacific (WP), which is consistent with the findings of Li (2014). The propagation characteristics and configuration of the MJO convection-circulation in the model are coincident with the observations over the first 15 days; however, as the forecast progresses, there are still several unrealistic elements in the model. For example, both the OLR and U850 anomalies in the model propagate faster than the observations, but appear to encounter barriers when reaching the MC (Maritime Continent) region and some of them propagate westwards. In the meantime, we see that the enhanced convection over WP is located in the east wind region of 850hPa; i.e., the opposite of the observations, which may be related to the faster eastward propagation of the MJO in the model.

To further compare the amplitude and propagation characteristics of the MJO between the observations and predictions, composite phase diagrams are generated for each initial phase and are shown in Fig. 6a for initial phases 1, 3, 5, and 7, and in Fig. 6b for initial phases 2, 4, 6, and 8. The composites are calculated when the observed MJO amplitude is greater than 1. The phase diagram is plotted for a 20-day target period with intervals of 5 days. Generally, the predicted amplitude and propagation of the MJO are consistent with the observations when the forecast initially starts from phases 2–4, but for other initial phases, the predicted propagation is faster, with the amplitude decaying rapidly after 10 day. This result is consistent with Fig. 2b, which shows that the MJO prediction skill is relatively higher when initiated from phases 2–4, but lower from phases 1 and 8. This also indicates the model prediction performance is not satisfied when the MJO signals move to the regions where climatological convection is depressed.

## 5. Predictability and uncertainty of RMM indices in the model

We examined the predictability of the MJO using the two estimation approaches described in Section 2. The average errors and signal estimates are shown in Fig. 7 as a function of lead time for initially strong and weak MJO cases, and also for all MJO cases. Following Neena et al. (2014), the single-member and ensemble-mean estimate of MJO predictability was obtained from the lead time at which each error curve becomes as large as the signal. For all cases (Fig. 7c), the signal increases sharply during the first six days of the hindcast and then decreases slowly with lead time, eventually being slightly lower than the climatological amplitude of the RMM indices ($RMM1^2 + RMM2^2 = 2$). The error grows quickly during the first 20 days, and reaches saturation after 40 days, by which time the single-member estimate error is 1.5 times greater than the ensemble-mean error. The estimated predictability for the single members is around 26 days, whereas the predictability for the ensemble mean is around 42 days. When comparing the strong and weak MJO cases, the results show a relatively clear difference, with the ensemble-mean predictability of the strong case being about3 days longer than that of the weak case.

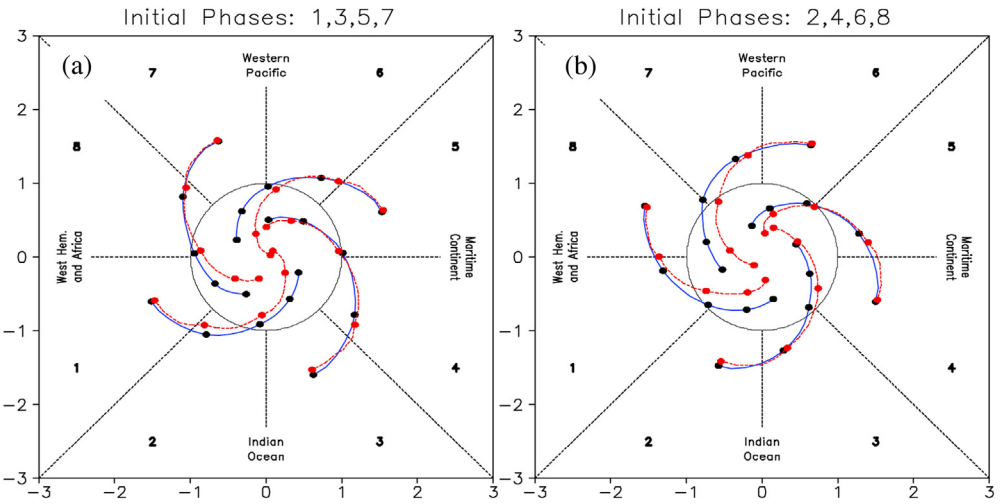


**Fig. 6.** Phase diagrams of the composite forecast for initial conditions with strong MJO (amplitude > 1). (a) Initial phases 1, 3, 5, and 7. (b) Initial phases 2, 4, 6, and 8. The composites were started from the observed values and the dots indicate the locations every five days. Blue curves are observations and red curves are the composite of the forecast (for interpretation of the references to color in this figure legend, the reader is referred to the web version of this article.)

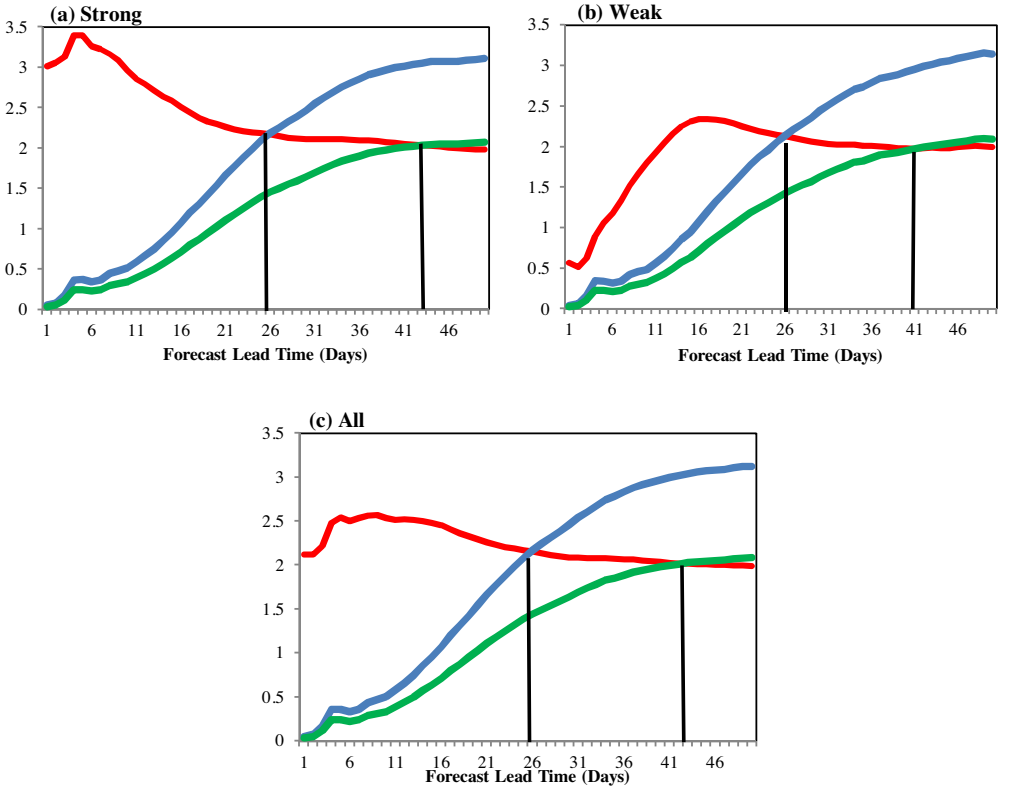


**Fig. 7.** Average error and signal estimates for strong (a), weak (b), and all (c) MJO initial conditions. Saturation of the blue solid error growth curve (single-member estimate) with respect to the signal (red) marks the MJO predictability for individual forecasts (denoted by the black vertical line), and saturation of the green solid error growth curve (ensemble-mean estimate) with respect to the signal (red dash) marks the MJO potential predictability for ensemble mean forecasts (for interpretation of the references to color in this figure legend, the reader is referred to the web version of this article.)

Here we are going to examine this dependence of MJO predictability on its initial phase (see Fig. 8). It is clear that the predictability is slightly higher when initialized from MJO phases 2–4 and 6, and this is consistent with the prediction skill shown in Fig. 2b. When examining the growth of error and signal separately, we find that the relatively higher predictability

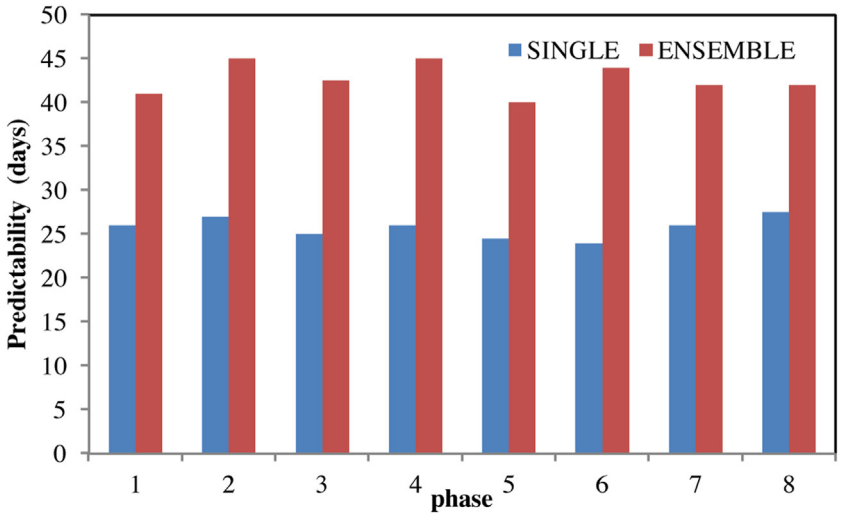


**Fig. 8.** Single-member and ensemble-mean estimates of MJO predictability (days) for the eight initial phases.

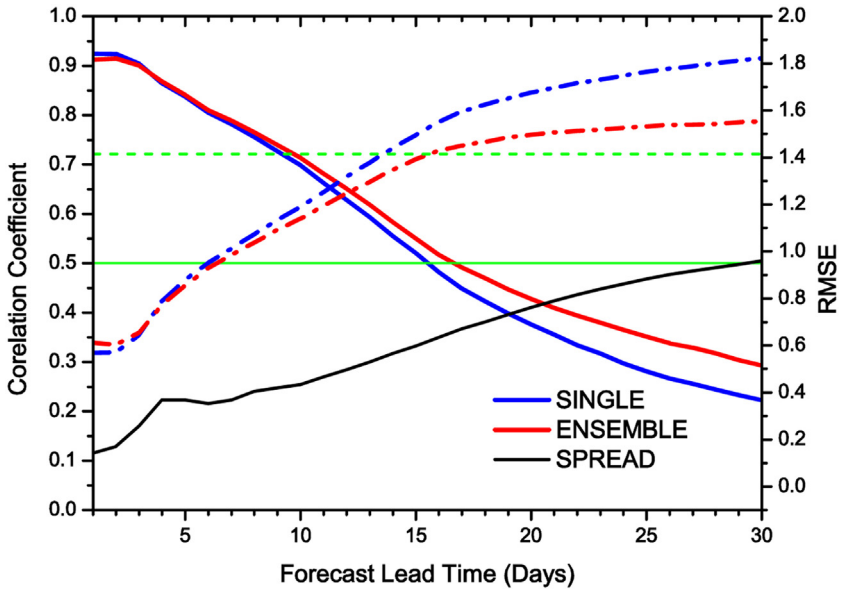


**Fig. 9.** Bivariate COR (solid line) and RMSE (dashed line) skill scores for the single member and ensemble mean of the RMM indices, showing the ensemble spread, which is plotted as a black solid line.

can be attributed to the larger signal in the forecasts initialized from phases 2–4. This further confirms that the increased predictability and prediction skills are most probably related to the stronger MJO convection signal over the Indian Ocean.

In addition, we also compared the single-member forecast skill with the ensemble-mean skill to quantitatively measure the benefits of the ensemble prediction system, and calculated the spread of the bivariate RMM indices for the ensemble forecasts to evaluate the uncertainty of the ensemble, which is defined as the combined standard deviations of the ensemble member hindcasts of RMM1 and RMM2, relative to their corresponding ensemble mean. Fig. 9 shows the bivariate COR and RMSE for single-member and ensemble-mean of the RMM indices, and the ensemble spread is also plotted. It can be seen that the single-member prediction skill for the MJO reaches about 14 days, and the ensemble mean has extended the prediction limit by about 2 days by increasing the COR and decreasing the RMSE as the forecast proceeds. However, the spread is much lower than the RMSE for all lead times, indicating that the ensemble spread is underdispersive for the MJO prediction, which may be associated with the inefficiency of the ensemble prediction system. We also notice that both the single-member and ensemble-mean predictability estimates are much higher than the present prediction skill, which indicate that BCC_AGCM2.2 still has room to improve its MJO prediction skill by up to 2 weeks before reaching the upper limit of predictability. The large gap between the single-member and ensemble-mean estimates implies that effective strategies for ensemble prediction would play a major role in the improvement of MJO forecasts.

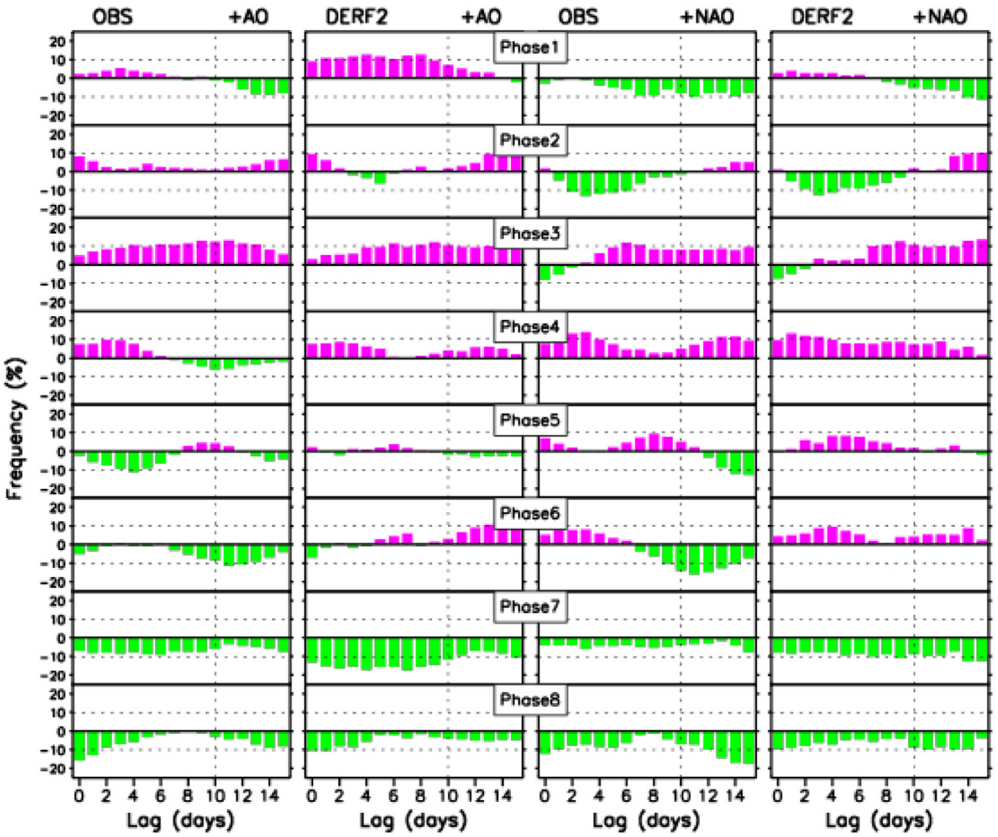


**Fig. 10.** Anomalous percentage occurrence of the positive AO and NAO regimes as a function of lag in days with respect to the MJO phases in the observations and BCC_AGCM2.2. The value of 0% means that the MJO phase was not discriminative for the regime whose occurrence is climatological. A value of 100% indicates that this regime occurs twice as frequently as its climatological mean, and −100% indicates no occurrence of this regime.

## 6. MJO impacts on northern hemisphere teleconnections

The implications of MJO prediction are mostly associated with subseasonal climate predictability through the direct impacts and indirect teleconnections of the MJO. Cassou (2008) showed that the MJO has a remote impact on the European weather regime, especially on the NAO and AO. In this section we will evaluate whether BCC_AGCM2.2 can reproduce the MJO impact on these Northern Hemisphere teleconnections.

Fig. 10 shows the lagged relationships between the MJO and AO/NAO for the reanalysis and hindcasts generated by BCC_AGCM2.2 during the extended boreal wintertime (November–March: NDJFM). Here, the AO and NAO modes are defined as the patterns of the first EOF of sea level pressure (SLP) over the Northern Hemisphere extratropical area (20–90°N) and Northern Atlantic region (80°W–40°E, 20–90°N), respectively, following Thompson and Wallace (2000) and Hurrell et al. (2003). These results show that the model is, to a large extent, able to capture the major lagged relationships between the MJO and AO/NAO. For instance, the probability of an AO/NAO+ event can be increased by more than 10% both in the model and observations about 10 days after an MJO phase 3 in which the deep convection is enhanced over the tropical Indian Ocean, and this is similar to the results of Cassou (2008). The lagged relationships in the model for phases 2, 4, 7, and 8 is also fairly consistent with the observations. However, the situation for phase 6 is opposite to the observations. Therefore, we further checked the MJO 10-day lagged composites of the Z500 anomalies for phases 3 and 6. In Fig. 11, there is an obvious wave train from the northern Pacific to the eastern coast of the North Atlantic for a 10-day lag of phase 3, which follows the wave ray path (Hoskins and Karoly, 1981), and then a positive significant NAO phase pattern can be detected over the North Atlantic region both in the observations and the model, although the amplitude of the anomalies is weaker in the model. However, the anomalous geopotential height patterns of the model hindcasts differ noticeably from the reanalysis over the North Atlantic region for phase 6; i.e., the positive geopotential height center over the Atlantic moves southwards, and is located at 40°N in the model compared with 60°N in the reanalysis data.

Fig. 12 shows the longitude–time plots of the lagged composites of daily Z500 anomalies averaged between 40°N and 60°N for phases 3 and 6 of the MJO. The lag composites for phase 3 are characterized by the Rossby wave train originating in the central Pacific, stretching across the North American continent, and propagating eastwards, accompanied by the eastward energy dispersion. The locations of the Z500 anomaly centers in the model are almost the same as in the observations,

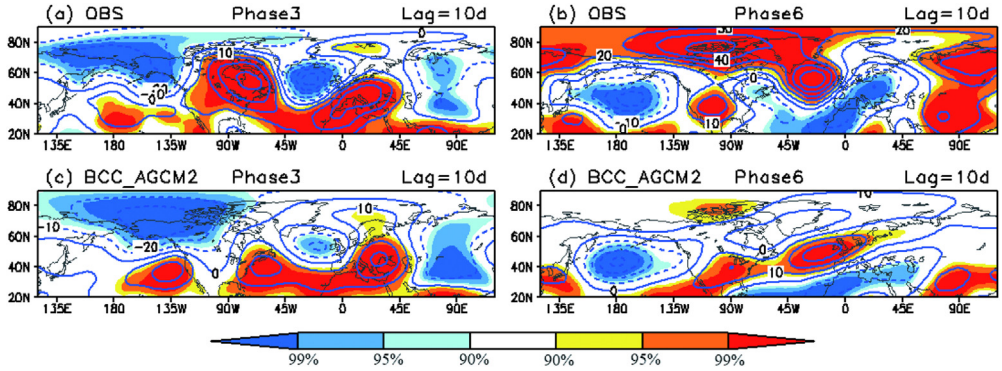


**Fig. 11.** MJO 10-day lagged composites of 500-hPa geopotential height anomalies in phase 3 for (a) observations and (c) BCC_AGCM2 hindcast. (b) and (d) as (a) and (c) but for phase 6. The contour interval is 10 gpm. The shaded areas mean the anomalies with the significance of student *t*-test at the 90%, 95%, and 99% confidence level, respectively.

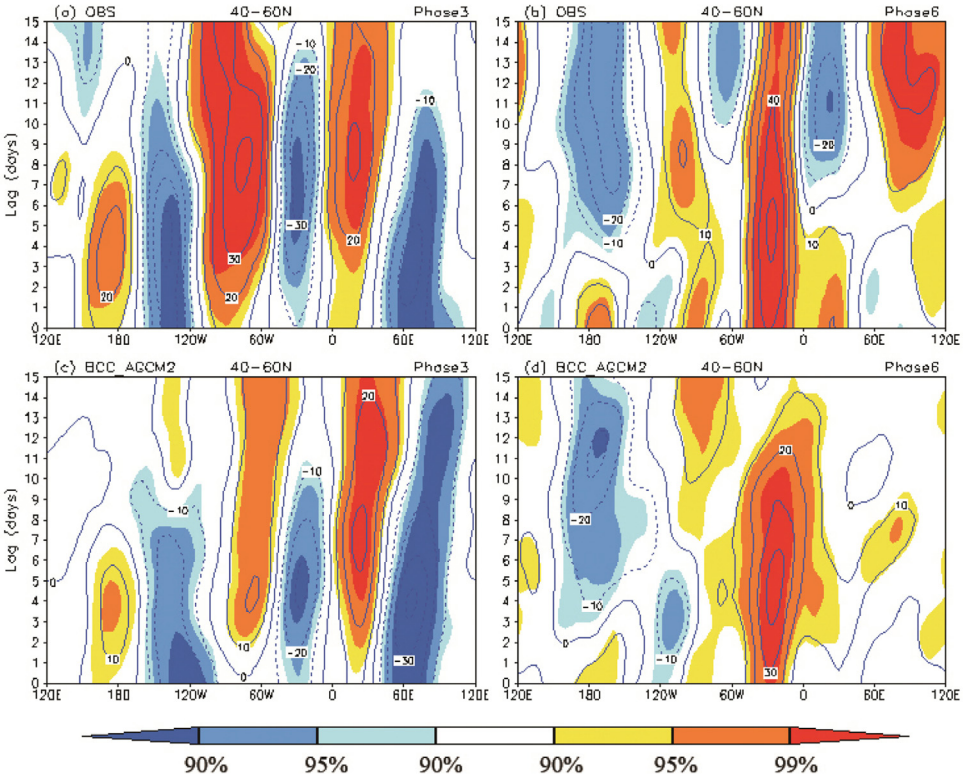


**Fig. 12.** Longitude–lag day cross sections of composites of daily Z500 anomalies averaged over 40°N–60°N in phases 3 (a, c) and phase 6 (b, d) of the MJO, where (a, b) are for observations and (c, d) for the BCC_AGCM2.2. The shaded areas mean the anomalies with the significance of student *t*-test at the 90%, 95%, and 99% confidence level, respectively.

although the speed of energy dispersion is a little faster. In contrast, for phase 6, there is no obvious signal coming from the Pacific and lack of westward energy propagation originating from Europe in the model. Cassou (2008) had deduced that the relationship between the MJO and an NAO+ event is more complicated, and is associated with the formation of Scandinavian blocking and flow–eddy interaction, which may be beyond the model's capability. However, it is clear that BCC_AGCM2.2 is capable of reproducing the main relationship between the MJO and AO/NAO, allowing for a significant extension of the potential predictability limit of these significant Northern Hemisphere weather regimes by about 2 weeks at least.

## 7. Conclusion and discussions

In this study, to comprehensively examine the performance of the BCC_AGCM2.2 model in predicting MJO, which is the most important predictability source over the subseasonal timescale, we evaluated the prediction skill, predictability, and teleconnection impacts of the MJO based on a hindcast dataset for the period 1991–2010. The MJO predictions in terms of the RMM indices are extracted by projecting the hindcast variables onto the observed combined EOFs, and the prediction skills are measured using the bivariate COR, RMSE, and MSSS methods. In addition, we also investigate the propagation characteristics, predictability, and extratropical teleconnection impacts of the MJO.

The useful MJO predictions generated by BCC_AGCM2.2 can reach 16–17 days at which point the RMM COR skill drops to 0.5, RMSE increases to $\sqrt{2}$, or MSSS drops to 0. This prediction skill, with no contribution from air–sea interaction, is comparable with other AGCMs worldwide, such as the NCEP GFS model. The prediction scores show a seasonal variation, with the highest skill in boreal autumn, especially in October when the prediction skill extends to 25 days. The prediction skills also vary as a function of the initial phase of the MJO; i.e., the COR skill is higher in phases 2–4 than in phases 1 and 8, which may be because the model is capable of maintaining a better MJO signal over the active convection region than over the Western Hemisphere.

We used two approaches to estimate MJO predictability in BCC_AGCM2.2: the single-member estimate and the ensemble-mean estimate. Our results show that MJO predictability is around 26 days for the single-member estimate and 42 days for the ensemble-mean estimate, which are comparable to other CGCM models, such as CFS and GFDL model (Neena et al., 2014; Xiang et al., 2015). A strong initial MJO condition can extend the predictability of the ensemble-mean estimate by about 3 days compared with the weak condition. The model also exhibits phase dependence, with a slightly higher predictability in hindcasts initiated from MJO phases 2–4, and this may be the result of better MJO signal maintenance in the model during these phases. However, the ensemble mean can extend the MJO skill by only about 2 days, which may be associated with the underdispersion in the ensemble prediction system.

For the teleconnection impacts of the MJO, we focused on evaluating the MJO—NAO lagged relationship, which is well reproduced by BCC_AGCM2.2. The lagged composite patterns of the 500-hPa geopotential height anomalies are fairly consistent with the observational patterns except that the model amplitude is weaker in phase 3. The model results clearly showed that the Rossby wave train originated in the central North Pacific and then stretched across the North American continent and propagated eastwards, and is accompanied by eastward energy dispersion. However, the MJO—NAO relationship of the model in phase 6 of MJO is significantly different to that seen in the observations, and this aspect requires further investigation.

We also note that some significant deficiencies exist in BCC_AGCM2.2 in the maintenance and propagation of the MJO, as follows. (1) The ensemble-mean MJO amplitude decreases too quickly. (2) The eastward propagation of MJO is faster and becomes less continuous than that seen in the reanalysis, typically over the MC and WP region, and the MJO structure over the WP is not well reproduced in the model, which may responsible for the quickly decreasing of the forecast skill during the time range of 20–40 days when compared with other model (Xiang et al., 2015). (3) The ensemble mean can only extend the prediction skill by two days, relative to the single members, and the estimated MJO predictability limit of this model (around 26 and 42 days)are much longer than the current prediction skill. These findings indicate that it will be extremely important to further develop the AGCM physics, especially the cumulus convection parameterization, and the model still has significant potential to improve its MJO predictions if we develop better ensemble strategies.

In addition, the prediction of the MJO is greatly influenced by the initial conditions (Fu et al., 2009, 2011; Ren et al., 2016). In this study, the BCC_AGCM2.2 model was initialized using the NCEP/NCAR Reanalysis-1 data. It has been pointed out that the intraseasonal variability of this data is much weaker than in reality, leading to the MJO amplitude being weaker than the observations over the first 3 days of the prediction period (Fig. 3b). Therefore, it is of great importance to improve the prediction skill of the model by optimizing the model initialization scheme and using the latest reanalysis data that incorporates better intraseasonal variability, such as the NCEP Climate Forecast System Reanalysis (CFSR, Saha et al., 2010) or the ERA-interim reanalysis data (Dee et al., 2011). These issues will be explored in future studies.

## Acknowledgements

This work was jointly supported by the National Basic Research (973) Program of China under Grant 2015CB453203, the China meteorological special project under Grant GYHY201406022, and the China National Science Foundation under Grant 41375062.

## References

Cassou, C., 2008. Intraseasonal interaction between the Madden-Julian oscillation and the north atlantic oscillation. Nature 455, 523–527.
Chou, C., Hsueh, Y.C., 2010. Mechanisms of northward propagating intraseasonal oscillation—a comparison between the Indian Ocean and the Western North Pacific. J. Clim. 23, 6624–6640.
Dee, D., et al., 2011. The ERA—interim reanalysis: configuration and performance of the data assimilation system. Quart. J. R. Meteorol. Soc. 137, 553–597.
Donald, A., Meinke, H., Power, B., Maia, A., de, H.N., Wheeler, M.C., White, N., Stone, R.C., Ribbe, J., 2006. Near-global impact of the Madden-Julian oscillation on rainfall. Geophys. Res. Lett. 33, http://dx.doi.org/10.1029/2005GL025155 (L09704).

Fu, X., Hsu, P., 2011. Extended-range ensemble forecasting of tropical cyclogenesis in the northern Indian Ocean: modulation of Madden-Julian oscillation. Geophys. Res. Lett. 38, http://dx.doi.org/10.1029/2011GL048249 (L15803).
Fu, X., Wang, B., Bao, Q., Liu, P., Lee, J.Y., 2009. Impacts of initial conditions on monsoon intraseasonal forecasting. Geophys. Res. Lett. 36, http://dx.doi.org/10.1029/2009GL037166 (L08801).
Fu, X., Wang, B., Lee, J.Y., Wang, W.Q., 2011. Sensitivity of dynamical intraseasonal prediction skills to different initial conditions. Mon. Weather Rev. 139, 2572–2592.
Fu, X., Lee, J.Y., Hsu, P.C., Taniguchi, H., Wang, B., Wang, W., Weaver, S., 2013. Multi-model MJO forecasting during DYNAMO/CINDY period. Clim. Dyn. 41, 1067–1081.
He, H., Li, Q., Wu, T., Tang, H., Hu, Z., 2014. Temperature and precipitation evaluation of monthly Dynamic Extended Range Forecast operational system DERF2.0 in China. Chin. J. Atmos. Sci. 38, 950–964 (in Chinese).
Hendon, H.H., 2000. Impact of air–sea coupling on the Madden–Julian oscillation in a general circulation model. J. Atmos. Sci. 57, 3939–3952.
Hoskins, B.J., Karoly, D.J., 1981. The steady linear response of a spherical atmosphere to thermal and orographic forcing. J. Atmos. Sci. 38, 1179–1196.
Hsu, P.C., Li, T., 2012. Role of the boundary layer moisture asymmetry in causing the eastward propagation of the Madden-Julian oscillation. J. Clim. 25, 4914–4931.
Hsu, P.C., Li, T., 2014. Moisture asymmetry and MJO eastward propagation in an aquaplanet general circulation model. J. Clim. 27, 8747–8760.
Hudson, D., Marshall, A.G., Yin, Y.H., Alves, O., Hendon, H.H., 2013. Improving intraseasonal prediction with a new ensemble generation strategy. Mon. Weather Rev. 141, 4429–4449.
Hurrell, J.W., Kushnir, Y., Visbeck, M., Ottersen, G., 2003. An overview of the North Atlantic Oscillation, in The North Atlantic Oscillation: Climatic significance and environmental impact. Geophys. Monogr. Ser. 134, edited by J.W. Hurrell et al., pp. 1–35, AGU, Washington, D. C.
Jeong, J.H., Kim, B.M., Ho, C.H., Noh, Y.H., 2008. Systematic variation in wintertime precipitation in East Asia by MJO-induced extratropical vertical motion. J. Clim. 21, 788–801.
Jia, X.L., Liang, X.Y., 2013. Possible impacts of Madden-Julian oscillation on the severe rain-snow weather in China during November 2009. J. Trop. Meteorol. 19, 233–241.
Jia, X.L., Chen, L.J., Ren, F.M., Li, C.Y., 2011. Impacts of the MJO on winter rainfall and circulation in China. Adv. Atmos. Sci. 28, 521–533.
Kalnay, E., et al., 1996. The NCEP/NCAR 40-year reanalysis project. Bull. Am. Meteorol. Soc. 77, 437–471.
Kang, I.S., Kim, H.M., 2009. Assessment of MJO predictability for boreal winter with various statistical and dynamical models. J. Clim. 23, 2368–2378.
Kang, I.S., Jang, P.H., Almazroui, M., 2014. Examination of multi-perturbation methods for ensemble prediction of the MJO during boreal summer. Clim. Dyn. 42, 2627–2637.
Kessler, W.S., Kleeman, R., 2000. Rectification of the Madden-Julian oscillation into the ENSO cycle. J. Clim. 13, 3560–3575.
Li, T., Zhou, C., 2009. Planetary scale selection of the Madden-Julian oscillation. J. Atmos. Sci. 66, 2429–2443.
Li, T., Zhao, C., Hsu, P.C., Nasuno, T., 2015. MJO initiation processes over the tropical Indian Ocean during DYNAMO/CINDY2011. J. Clim. 28, 2121–2135.
Li, T., 2014. Recent advance in understanding the dynamics of the Madden-Julian oscillation. J. Meteorol. Res. 28, 1–33.
Liebmann, B., Smith, C.A., 1996. Description of a complete (interpolated) outgoing longwave radiation dataset. Bull. Am. Meteorol. Soc. 77, 1275–1277.
Lin, H., Brunet, G., Derome, J., 2008. Forecast skill of the Madden–Julian oscillation in two Canadian atmospheric models. Mon. Weather Rev. 136, 4130–4149.
Madden, R.A., Julian, P.R., P.R, 1971. Detection of a 40–50 day oscillation in the zonal wind in the tropical Pacific. J. Atmos. Sci. 28, 702–708.
Madden, R.A., Julian, P.R., P.R, 1972. Description of global-scale circulation cells in the tropics with a 40–50 day period. J. Atmos. Sci. 29, 1109–1123.
Neena, J.M., Lee, J.Y., Waliser, D., 2014. Predictability of the Madden–Julian oscillation in the intraseasonal variability hindcast experiment (ISVHE). J. Clim. 27, 4531–4543.
Pegion, K., Kirtman, B., 2008. The impact of air–sea interactions on the predictability of the tropical intraseasonal oscillation. J. Clim. 21, 5870–5886.
Qi, Y., Zhang, R., 2015. A review of the intraseasonal oscillation associated with rainfall over eastern China and its operational application. J. Trop. Meteorol. 31, 556–576 (in Chinese).
Rashid, H.A., Hendon, H.H., Wheeler, M.C., Alves, O., 2011. Prediction of the Madden–Julian oscillation with the POAMA dynamical prediction system. Clim. Dyn. 36, 649–661.
Ren, H.L., Wu, J., Zhao, C., Liu, Y., Jia, X., Zhang, P., 2015. Progresses of MJO prediction researches and developments. J. Appl. Meteorol. Sci. 26, 658–668 (in Chinese).
Ren, H.L., Wu, J., Zhao, C., Cheng, Y., Liu, X., 2016. MJO ensemble prediction in BCC-CSM1.1(m) using different initialization schemes. Atmos. Oceanic Sci. Lett. 9, 60–65.
Saha, S., et al., 2010. The NCEP climate forecast system reanalysis. Bull. Am. Meteorol. Soc. 91, 1015–1057.
Seo, K.H., Wang, W., Gottschalck, J., Zhang, Q., Schemm, J.K.E., Higgins, W.R., Kumar, A., 2009. Evaluation of MJO forecast skill from several statistical and dynamical forecast models. J. Clim. 22, 2372–2388.
Shukla, J.S., 2000. Dynamical seasonal prediction. Bull. Am. Meteorol. Soc. 81, 2593–2606.
Thompson, D.W.J., Wallace, J.M., 2000. Annular modes in the extratropical circulation. Part I: month-to-month variability. J. Clim. 13, 1000–1016.
Vitart, F., Molteni, F., 2010. Simulation of the MJO and its teleconnections in the ECMWF forecast system. Quart. J. R. Meteorol. Soc. 136, 842–855.
Vitart, F., Woolnough, S., Balmaseda, M.A., Tompkins, A.M., 2007. Monthly forecast of the Madden–Julian oscillation using a coupled GCM. Mon. Weather Rev. 135, 2700–2715.
Vitart, F., Leroy, A., Wheeler, M.C., 2010. A comparison of dynamical and statistical predictions of weekly tropical cyclone activity in the southern hemisphere. Mon. Weather Rev. 138, 3671–3682.
Vitart, F., 2014. Evolution of ECMWF sub-seasonal forecast skill scores. Quart J. R. Meteorol. Soc. 140, 1889–1899.
Waliser, D., et al., 2006. The experimental MJO prediction project. Bull. Am. Meteorol. Soc. 87, 425–431.
Wang, W., Chen, M., Kumar, A., Xue, Y., 2011. How important is intraseasonal surface wind variability to real-time ENSO prediction? Geophys. Res. Lett. 38, http://dx.doi.org/10.1029/2011GL047684 (L13705).
Wang, W., Hung, M.P., Weaver, S.J., Kumar, A., Fu, X., 2014. MJO prediction in the NCEP climate forecast system version 2. Clim. Dyn. 42, 2509–2520.
Wheeler, M., Hendon, H.H., 2004. An all-season real-time multivariate MJO index: development of an index for monitoring and prediction. Mon. Weather Rev. 132, 1917–1932.
Wu, T.W., Yu, R.C., Zhang, F., Wang, Z., Dong, M., Wang, L., Jin, X., Chen, D., Li, L., 2010. The Beijing climate center for atmospheric general circulation model (BCC AGCM 2.0.1): description and its performance for the present-day climate. Clim. Dyn. 34, 123–147.
Xiang, B., Zhao, M., Jiang, X., Lin, S.J., Li, T., Fu, X., 2015. The 3–4 week MJO prediction skill in a GFDL coupled model. J. Clim. 28, 5351–5364.
Zhang, C., 2005. Madden-Julian oscillation. Rev. Geophys. 43, RG2003, http://dx.doi.org/10.1029/2004RG000158.
Zhang, C., 2013. Madden-Julian oscillation—bridging weather and climate. Bull. Am. Meteorol. Soc. 94, 1849–1870.
Zhao, C., Li, T., Zhou, T., 2013. Precursor signals and processes associated with MJO initiation over the tropical Indian Ocean. J. Clim. 26, 291–307.
Zhao, C., Zhou, T., Song, L., Ren, H., 2014. The boreal summer intraseasonal oscillation simulated by 4 Chinese AGCMs participated in CMIP5 project. Adv. Atmos. Sci. 31, 1167–1180.
Zhao, C., Ren, H.L., Song, L., Wu, J., 2015. Madden-Julian oscillation simulated in BCC climate models. Dyn. Atmos. Oceans 72, 88–101.
Zuo, J., Ren, H.L., Wu, J., Nie, Y., Li, Q., 2016. Subseasonal variability and predictability of the Arctic Oscillation/North Atlantic oscillation in BCC_AGCM2.2. Dyn. Atmos. Oceans 75, 33–45.